Geomechanics and Engineering, *Vol. 41, No. 4 (2025) 429-442*
https://doi.org/10.12989/gae.2025.41.4.429

Morphology and distribution characteristics of tunnel bearing arch in horizontal layered surrounding rock

Pengtao Chen[1,2], Junru Zhang*[1,2], Jianchi Ma[1,2], Kaimeng Ma[1,3], Yi Dai[1,2], Tong Pan[1,2] and Zhiyi Jin[1,4]

[1]*School of Civil Engineering, Southwest Jiaotong University, No 111, Section 1 North, Second Ring Road, Chengdu 610031, China*
[2]*Key Laboratory of Transportation Tunnel Engineering, Ministry of Education, Southwest Jiaotong University, No 111, Section 1 North, Second Ring Road, Chengdu 610031, China*
[3]*School of Civil Engineering, Shijiazhuang Tiedao University, No. 17, North Second Ring East Road, Shijiazhuang 050043, China*
[4]*College of Civil Engineering and Architecture, Xinjiang University, No. 777, Huarui Street, Urumqi 830047, China*

(*Received October 7, 2023, Revised May 7, 2025, Accepted May 8, 2025*)

Abstract. Tunnel excavation induces stress redistribution in the surrounding rock, forming a bearing arch to sustain ground stress. As a typical and special type of rock formation, the bearing arch morphology in (approximately) horizontally layered surrounding rock remains unclear due to the influence of structural planes. Additionally, the effects of factors such as ground stress, layer thickness, and interlayer contact conditions on the distribution of the bearing arch are not well understood. To address this issue, non-contact strain acquisition experiments combined with numerical calculations were used to determine the morphology of the bearing arch, followed by sensitivity analysis of the parameters. The results indicate that non-uniform rock masses under unfavorable stress conditions may fail at stress levels far below the ultimate strength of the rock blocks. For tunnels excavated in horizontally layered surrounding rock, vertical loads easily cause bending-induced tensile stress in the roof and floor, while increasing initial horizontal stress improves the bearing condition. The bearing arch in horizontally layered surrounding rock exhibits two extreme states after excavation: "butterfly-shaped" and "rounded rectangular." Under extreme conditions, "bearing zone discontinuity" may occur in the vertical direction. Overall, the lateral pressure coefficient and interlayer bonding strength significantly influence the bearing arch, while the layer thickness has a relatively smaller effect. The lateral pressure coefficient mainly affects the arch's morphology, while interlayer bonding strength and layer thickness primarily influence the stress redistribution during the post-excavation stress equilibrium process. In practical tunnel engineering, engineering measures should aim to enhance the overall integrity of the surrounding rock to fully utilize the bearing arch effect.

Keywords: bearing arch; distribution characteristics; horizontal layered surrounding rock; influencing factors; morphology characteristics; tunnel excavation

1. Introduction

In China, extensive transportation infrastructure projects often encounter complex geological conditions, particularly in the southwest region where horizontally layered sedimentary rocks such as mudstone, sandstone, and shale are prevalent. These formations exhibit significant anisotropy in their physical and mechanical properties due to horizontal or gently inclined layering. Consequently, tunneling in such strata frequently leads to challenges like rock peeling, bending, deformation of support structures, and uplift of the tunnel bottom (Do *et al*. 2019, Ma *et al.* 2022).

During tunnel excavation in horizontally layered rock, inadequate handling or the lack of timely construction intervention can result in rock cracking and instability at the contact surfaces. These combined effects can easily lead to collapse and damage at the tunnel roof (Yuan *et al.* 2022, Małkowski 2015, Moussaei *et al.* 2019, Yang *et al.* 2017). Yang *et al.* (2016), based on the Hoek-Brown strength theory, studied the collapse shape of tunnel roofs in layered rock masses. Using the upper bound theorem and variational principle, they derived the roof collapse volume and analyzed the influence of various parameters on the failure mechanism. Khezri *et al.* (2016) improved the three-dimensional kinematic admissible failure mechanism to simulate layered soil and used the upper bound limit theorem to examine the three-dimensional stability of shallow circular tunnels in layered soil. Chen *et al*. (2021) proposed a new classification criterion for large deformations based on the power-exponential variation rule of the deformation-to-strength stress ratio for the large extrusion deformation mechanism of layered soft rock tunnels under high geostress. They introduced the initial damage tensor, reflecting the distribution of nodal joints, and an equivalent damage evolution equation derived from viscoplastic strain, to establish a rheological damage model for layered soft rock. Qi *et al.* (2021) analyzed the deformation characteristics of roadways in layered surrounding rock by combining monitoring techniques and discrete element numerical simulation. They proposed a suitable method for controlling the deformation of tunnel perimeter rock, considering the construction parameters of anchors.

*Corresponding author, Professor
E-mail: jrzh@swjtu.edu.cn

Copyright © 2025 Techno-Press, Ltd.

ISSN: 2005-307X (Print), 2092-6219 (Online)

The bearing arch hypothesis was first proposed by Hack and Gillitzer in the last century. They suggested that in mining engineering, a "bearing arch" forms during the self-stabilization of the rock mass above the mining area following excavation disturbances (Brady *et al.* 1985). This concept was later introduced to tunnel engineering. The unloading disturbances caused by tunnel excavation induce a redistribution of stress within the surrounding rock, aiming to reach a state of stress equilibrium after excavation. During this stress redistribution process, the surrounding rock naturally stabilizes by adjusting its displacement and deformation. A notable manifestation of this phenomenon is the formation of a bearing arch within the rock around the tunnel excavation contour (Wang *et al*. 2022). Existing studies have pointed out that the shape of the tunnel cross-section, the initial principal stress direction, and the rock mass structural planes are key factors influencing the rock's self-bearing capacity (Chen *et al.* 2024).

Focusing on the bearing arch effect during tunnel excavation in layered surrounding rock, Zhao *et al*. (2021) used similarity model tests to analyze the stress evolution characteristics, stress arch distribution, and failure patterns of three types of rock masses: intact, layered, and blocky. They further explored the failure mechanisms and bearing capacities of the surrounding rock. By fully leveraging the potential of the bearing arch effect during the design and construction phases, tunnel support parameters can be precisely controlled, ensuring both construction and operational safety. This approach helps avoid unnecessary material waste and reduces carbon emissions associated with tunnel boundary support and lining (Rodriguez et al., 2021). Such practices align with the global emphasis on low-carbon development.

Currently, most scholarly research on bearing arches in practical applications (Pardo *et al*. 2014, Ma *et al*. 2022, Li *et al*. 2023, Tan *et al*. 2014, Jin *et al*. 2018, Huang *et al*. 2021, Zhu *et al*. 2022, Man *et al*. 2022) primarily focuses on laboratory testing and numerical simulations. While studies on homogeneous rock formations have reached a more advanced stage, there is a noticeable lack of research on the formation process and morphological characteristics of load-bearing arches in tunnels within layered (non-homogeneous) surrounding rock. Additionally, the effects of parameters such as layer thickness, inclination, and interlayer bonding strength on bearing arches have been seldom explored.

Building on this research context, this paper investigates the formation process and morphological characteristics of bearing arches in horizontally layered surrounding rock tunnels. Through observational experiments, in-depth analysis, and numerical simulations, the study aims to elucidate the morphological traits and distribution patterns of these load-bearing arches. The findings of this research aim to provide valuable insights for the design and construction of tunnel projects.

2. Theoretical definition of tunnel bearing arch

Existing studies indicate that for tunnels with the same cross-sectional area, the difference in cross-sectional shape has little impact on the plastic zone of the surrounding rock after excavation. Therefore, for ease of analysis, a circular cross-sectional shape is adopted for subsequent studies (Lin *et al.* 2022). According to classical elastoplastic theory, after tunnel excavation, a stress redistribution zone forms within a certain range around the tunnel. When the surrounding rock stress reaches the yield strength, it enters the plastic zone. With further stress redistribution, the rock mass deforms and extrudes toward the free surface, gradually releasing the stress in the plastic zone. As shown in Fig. 1, the region around the tunnel where the tangential stress exceeds the initial in-situ stress before excavation is considered the load-bearing zone of the surrounding rock. The surrounding rock closer to the excavation boundary, where the tangential stress is lower than the initial in-situ stress, is classified as the non-load-bearing zone (Brown 1980).

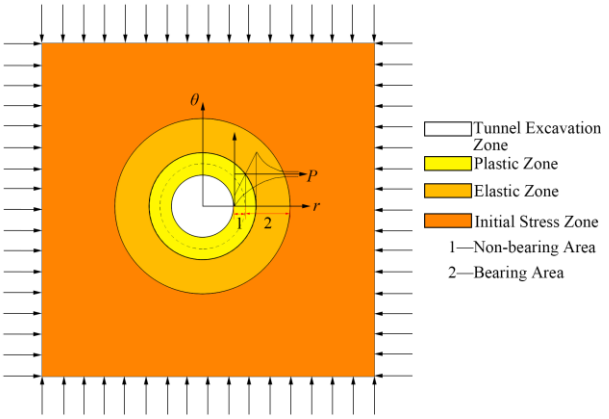

Fig. 1 Stress state of elastic-plastic surrounding rock

Based on the Mohr-Coulomb damage criterion, the rock mass experiences plastic deformation according to the following criterion

$$\begin{cases} \sigma_{tp} - \xi\sigma_{rp} - R_b = 0 \\ \xi = \dfrac{1+\sin\theta}{1-\sin\theta} \end{cases} \tag{1}$$

Where: σ_{tp} is the tangential stress in the plastic zone; σ_{rp} is the radial stress in the plastic zone; R_b is the uniaxial compressive strength of the surrounding rock; θ is the angle of internal friction of the surrounding rock; ξ is the slope of the intensity line according to Mohr-Coulomb.

The state of stress within the plastic zone is

$$\begin{cases} \sigma_{rp} = \dfrac{R_b}{\xi-1}\left[\left(\dfrac{r}{r_0}\right)^{\xi-1} - 1\right] \\ \sigma_{tp} = \dfrac{R_b}{\xi-1}\left[\left(\dfrac{r}{r_0}\right)^{\xi-1}\xi - 1\right] \end{cases} \tag{2}$$

Where: r_0 is the radius of the circular tunnel; r is the distance from a point in the surrounding rock to the centre of the tunnel.

The analysis above underscores that the surrounding rock serves as both the origin and conveyer of tunnel loads. During tunnel excavation, the rock is compressed into the

cavity due to unloading effects, acting as a load source. Simultaneously, the rock autonomously adapts by forming a load-bearing zone as it resists deformation. The inherent load-bearing capacity of the surrounding rock significantly influences tunnel stability. The bearing zone exhibits heightened tangential stresses to withstand radial loading, akin to the force distribution in an arch bridge. This phenomenon is often referred to as the "bearing arch" due to its resemblance to arch bridge mechanics. For the sake of simplifying analysis, the stress-bearing zone and its extent are defined using the widely-accepted tangential stress criterion (Ma *et al.* 2024, Lin *et al*. 2022, Hoek *et al.* 1980), as expressed in Eq. (3). Specifically, when the load-bearing ratio is below 0, the area is categorized as non-bearing; conversely, when the load-bearing ratio exceeds 0, it falls under the bearing zone. At the inner boundary of the bearing zone, $D_\sigma = 0$, while at the outer boundary, $D_\sigma = 10\%$.

$$D_\sigma = \frac{\sigma_\theta - \sigma_\theta^0}{\sigma_\theta^0} \times 100\% \tag{3}$$

Where: D_σ is the stress bearing capacity; σ_θ is the tangential stress; σ_θ^0 is the initial tangential stress.

The tangential stress is determined using the polar transformation equation

$$\sigma_\theta = \frac{\sigma_x + \sigma_z}{2} - \frac{\sigma_x - \sigma_z}{2}\cos 2\theta - \tau_{xz}\sin 2\theta \tag{4}$$

Where: σ_x is the horizontal stress; σ_z is the vertical stress; τ_{xz} is the shear stress.

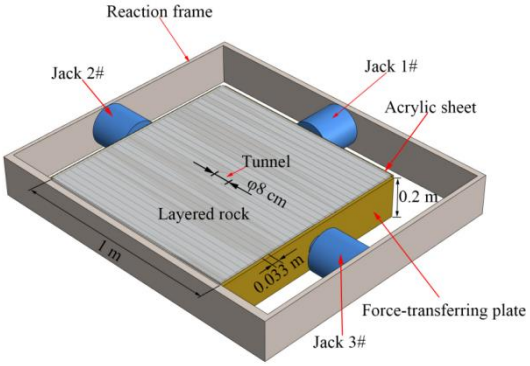

(a) Schematic of the loading device

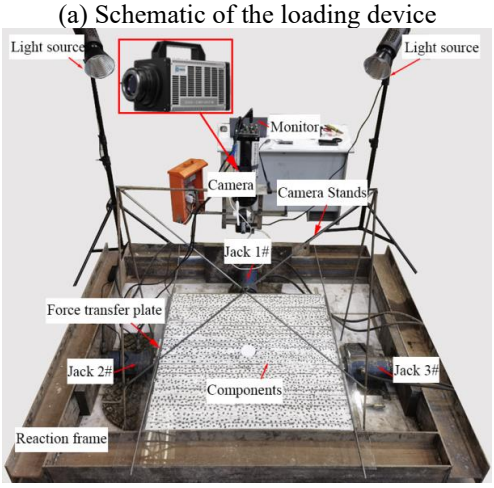

(b) On-site photo

Fig. 2 Test equipment

3. Morphological characteristics of bearing arches in tunnels excavated in horizontally layered rock

Building upon the elastic-plastic theoretical framework and the load-bearing arch determination criteria discussed in the previous section, this segment aims to analyze the morphological traits of load-bearing arches in tunnels excavated through horizontally layered rock formations. This analysis will be conducted through a combination of phenomenological testing and numerical simulations.

3.1 Bearing arch testing

The objective of this test is to manipulate the orientation of the principal stress relative to the joint directions by modifying the load distribution along both perpendicular and parallel joint surfaces. This allows for the observation of the surrounding rock's load-bearing behavior under various conditions. In polar coordinates, the minimum principal stress (positive in tension) can offer insights into the shear stress patterns around the tunnel. Therefore, the formation of the load-bearing arch in horizontally layered surrounding rock is determined by assessing the concentration of minimum principal strain.

3.1.1 Design of the test

The experimental setup comprises two main components: the loading system and the measurement system. The model loading configuration is depicted in Fig. 2(a). The loading system comprises three jacks, three force-transmitting steel plates with a thickness of 1.5cm each, and reaction frames. The experiment was devised to acquire surface strain data from the specimen and was executed through horizontal loading, without accounting for the influence of gravity. The specimen's surface was secured using acrylic plates and steel bars to restrict vertical displacement, ensuring a plane strain configuration. Additionally, each jack maintained contact with the force-transmitting steel plate, facilitating load transfer to the specimen.

The measurement system encompasses a high-speed camera, camera mount, two light sources, and a monitor. The strain measurement for this test employs the XTDIC three-dimensional full-field deformation measurement and analysis system. This system involves applying optical speckles onto the specimen's surface and using a high-speed camera to capture speckle images throughout the entire loading process. By employing Digital Image Correlation (DIC) algorithms, parallax data of points on the observation object's surface is obtained. This data is then used to reconstruct the coordinates of the surface speckles, allowing for a comparison of speckle coordinate differences within the measurement area. This comparison yields the displacement field of the observation object's surface, which in turn enables the determination of the strain field. A photograph of the test system setup is depicted in Fig. 2(b).

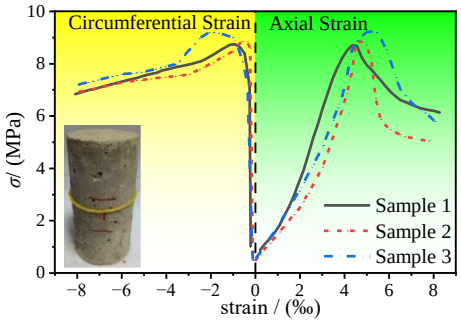

Fig. 3 Stress state of elastic-plastic surrounding rock

3.1.2 Test material

Due to the challenges of preparing low-strength and thin-layered specimens, such as low casting efficiency, difficulty in compaction, and poor molding, as well as the high risk of damage during curing and handling, these materials are unsuitable for supporting this experiment under limited conditions. Therefore, cement mortar was used as the simulation material for this experiment.

Cylindrical specimens with dimensions of 50 mm (diameter) × 100 mm (height) were prepared, and the stress-strain curves for several specimens under uniaxial compression are shown in Fig. 3. The results indicate: The average peak strength of the three groups of specimens is 8.98 MPa; The average elastic modulus is 1.79 MPa. The peak axial strain is approximately 4.5×10^{-3}.

The uniaxial compression characteristic curves of the three groups of specimens are similar, showing an initial increase in stress with strain, reaching a peak, and then gradually declining to the residual failure state. This confirms that the specimens exhibit elastoplastic mechanical properties and are suitable for use in this experiment.

3.1.3 Test procedure

Prior research (Guo *et al*. 2021, Lei *et al.* 2015) has highlighted that the distribution of tangential stresses within the surrounding rock, induced by excavation unloading, bears resemblance to the tangential stress values derived from the loading test results on pre-drilled holes. Moreover, these stress values exhibit an analogous distribution pattern. As elucidated in Section 2, the assessment of the bearing arch hinges on the variation in tangential stress within the surrounding rock prior to and following excavation. This involves utilizing the tangential stress present in the perimeter rock before excavation as a reference point. The tangential stress encountered after excavation is then subtracted from the tangential stress observed before excavation, yielding the disparity between the two states. Considering the sensitivity of the DIC system to image interference, excavation holes are strategically incorporated during the component casting phase to avoid disruptions from post-loading cutting and coring activities. This ensures accurate image recognition and analysis. The test program and steps are summarized as follows:

(1) Working conditions setting

Due to challenges encountered during the preparation of the low-strength and thinly layered test block, including issues like inefficient pouring, challenging vibration, and complex molding, along with risks of cracking and crushing during maintenance and lifting, conducting the test under constrained circumstances became problematic. To address these constraints, M10 mortar is employed as a substitute material in this test. Four primary sets of working conditions were established. The control group consisted of homogeneous surrounding rock, as outlined in Table 1.

Table 1 Model test conditions

Condition No.	Rock types	Lateral pressure coefficient	Direction of principal stress	Oil pressure(t)	
				Jack 1#	Jack 2#, 3#
A	Homogeneous	1	Asymmetrical	5	5
				10	10
B	Layered	0.5	Vertical（perpendicular to joints）	5	2.5
				10	5
C	Layered	1	Asymmetrical	5	5
				10	10
D	Layered	1.5	Transverse (parallel to joints)	5	7.5
				10	15

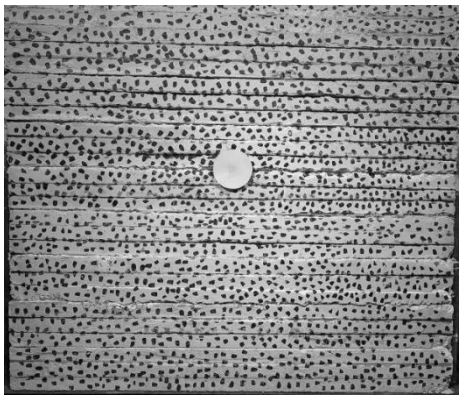

(a) Layered rock components

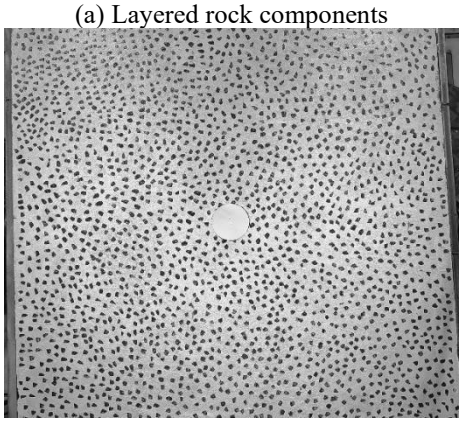

(b) Homogeneous rock component

Fig. 3 Completed components

(2) Test development

Taking into account site conditions, the complexity of model casting, and adherence to the Saint-Venant principle to minimize boundary effects, we cast single-layer

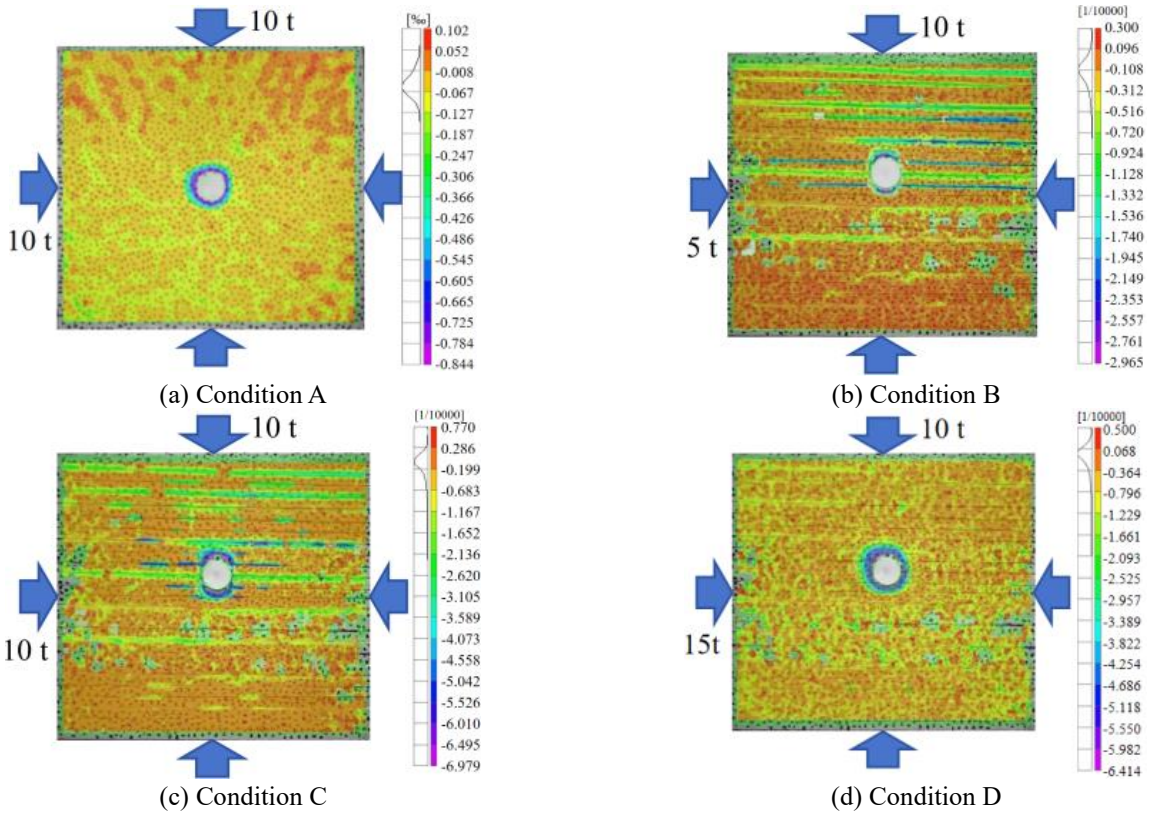

Fig. 4 Contour plots of minimum principal strain in experimental results

components for the layered surrounding rock at dimensions of 1 m × 0.033 m × 0.2 m, while the homogeneous rock components were cast at dimensions of 1 m × 1 m × 0.2 m. Within the formwork, we reserved a cavity space with an 8 cm diameter, completed the casting, and conducted the necessary maintenance. Subsequently, we applied water-based white paint for priming and used black ink for scattering to achieve the components shown in Fig. 4.

After the components are completed, they are placed into the loading device. Before loading, white cardboard is used to create circular disks of the same size as the cavities to cover the cavity positions. Once the installation is complete, the loading process begins. The corresponding jacks for each working condition are gradually loaded as shown in Table 1. After each loading reaches the target oil pressure, the loading is paused for 5 minutes, and continuous video recording is conducted at each stage.

After the completion of loading, image sequences were exported from the FastPhoto system to the XTDIC software. In the XTDIC software, a planar grid was established, seed points were set for calibration and positioning across different images in the image sequence. Additionally, two-dimensional parameters such as scaling and projection thresholds were configured for the cameras. Once these settings were properly adjusted, image processing and calculations were performed.

3.1.4 Test results

Test image sequences are compared and analyzed to assess the outcomes of the most significant working conditions across various principal stress directions.

The minimum principal strain results for the component at the highest loading level under various working conditions are shown in Fig. 5.

From the Fig. 5, it can be observed that in Condition A, where the surrounding rock is homogeneous and the principal stress direction is symmetrical, there is a significant concentration of compressive strain around the tunnel perimeter. In areas far from the tunnel, there is some tensile strain, but its magnitude is much smaller than the concentrated compressive strain around the tunnel. The distribution of compressive strain around the tunnel is relatively uniform, and the various directions in the bearing zone show a consistent pattern.

Conditions B to D represent horizontally layered surrounding rock with a gradual change in the direction of the principal stress. When the principal stress direction is perpendicular to the joint surface (Condition B), there is significant squeezing deformation in the interlayer joints, with pronounced vertical squeezing deformation around the tunnel. The distribution of compressive strain around the tunnel corresponds to the direction of the principal stress.

In the case where the principal stress direction is symmetrical (Condition C), A the tension in the joints of the component intensifies, while the squeezing weakens.

Compressive strain concentration around the tunnel's top and bottom slabs becomes more significant, extending to the left and right sides. Due to the presence of interlayer joints, the minimum principal strain around the tunnel primarily occurs at the crown and invert, demonstrating a distribution perpendicular to the joint orientation.

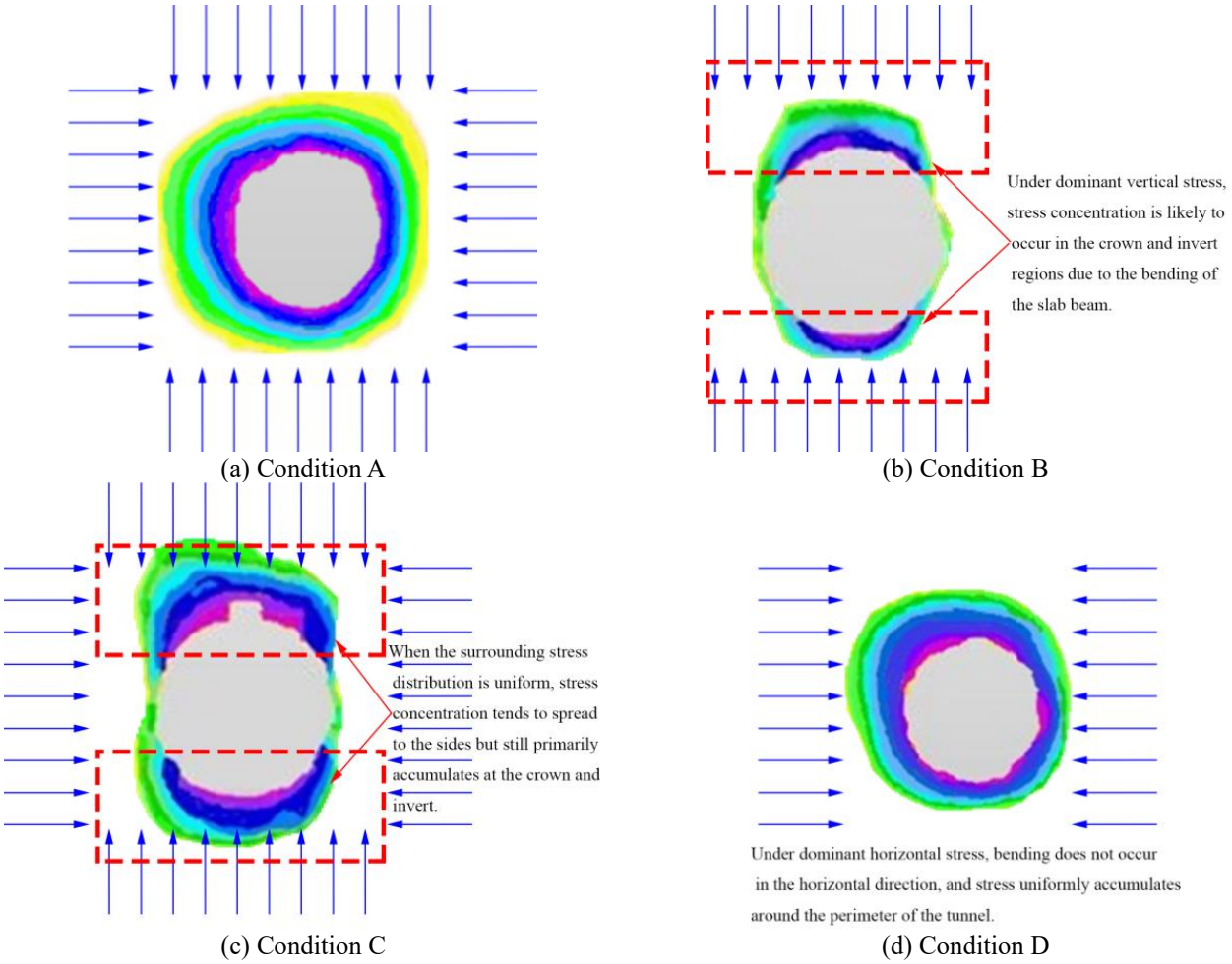

(a) Condition A (b) Condition B

(c) Condition C (d) Condition D

Fig. 5 Local detail of the minimum main strain around the hole

When the principal stress direction is parallel to the joint surface (Condition D), tension occurs in the interlayer joints, and the principal stress direction around the tunnel is predominantly compressive. The compressive strain distribution extends more significantly to the left and right sides compared to the first two conditions, and the strain concentration pattern resembles a rounded square.

The extracted local detailed strain maps around the tunnel for each test condition are shown in Fig. 6. Comparing the minimum principal strain results between Condition A and Condition C, there is a significant difference in strain distribution around the tunnel between homogeneous rock and layered rock under the same loading conditions. When the principal stress direction is symmetrical, the stress concentration around the tunnel in the homogeneous rock tunnel is relatively evenly distributed. In contrast, in the layered rock tunnel, compressive strain is more concentrated towards the top and bottom slabs. The top and bottom slabs bear more stress near these positions, indicating that these areas are the weakest points of the load-bearing arch, representing the most unfavorable conditions.

Comparing the minimum principal stress results for Conditions B to D, as the principal stress direction changes from vertical to horizontal, and the initial lateral pressure coefficient gradually increases, strain concentration gradually spreads to both sides around the tunnel. The sidewalls gradually bear more stress. When the initial stress direction is parallel to the joints, strain around the tunnel becomes relatively evenly distributed, indicating that for tunnel excavation in horizontally layered surrounding rock, vertical loads are the most unfavorable. The top and bottom slabs are more likely to experience stress concentration. An increase in initial horizontal stresses will lead to the sidewalls bearing more stress, which is more favorable for the formation of load-bearing arches near the top and bottom slabs, providing some improvement.

3.2 Numerical modelling studies

The earlier phase observed the strain distribution characteristics of the surrounding rock after tunnel excavation through experimental tests, analyzing and inferring the load-bearing characteristics of layered surrounding rock tunnels compared to homogeneous surrounding rocks. However, the results did not directly reflect the distribution of the load-bearing arch. Therefore, numerical simulation studies will be conducted to further determine the form and distribution characteristics of the load-bearing arch in layered surrounding rock tunnels.

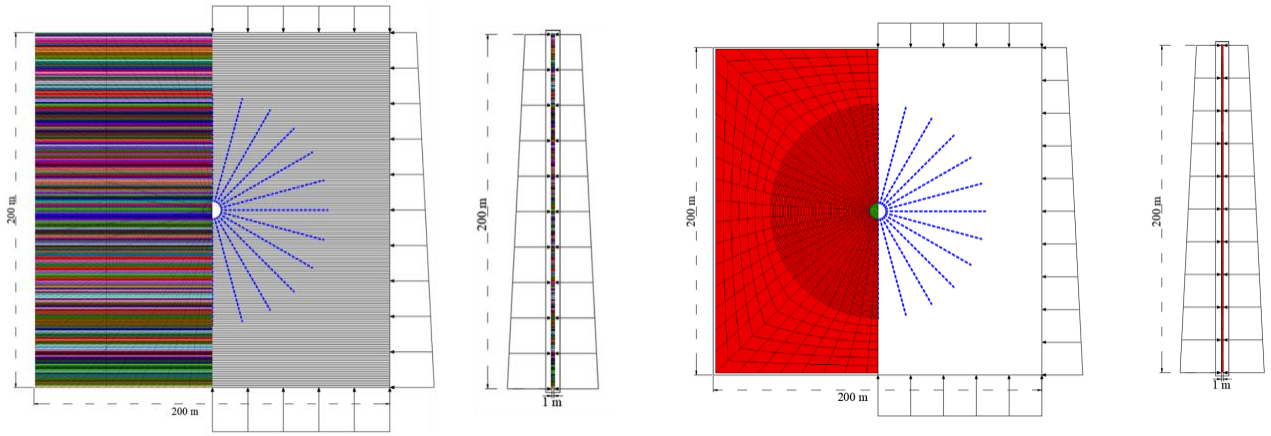

(a) Model of horizontal layered surrounding rock (b) Model of homogeneous surrounding rock

Fig. 6 Schematic diagrams of numerical models

3.2.1 Model setup

Due to the segmentation of stratified surrounding rock by joints, its mechanical behavior is influenced by the properties of the joints, leading to significant differences compared to homogeneous rock. The discrete element method (DEM) is particularly suitable for studying deformation and failure phenomena caused by different continuous interfaces. Therefore, in this study, the stratified rock mass model is constructed using the discrete element software 3DEC. Additionally, to highlight the load-bearing arch characteristics in tunnel excavation of stratified surrounding rock, a homogeneous rock mass model is established using the finite difference software FLAC3D for comparative analysis. The model configurations are shown in Fig. 7.

Corresponding to the theoretical analysis presented earlier, the calculation for layered surrounding rock uses the Mohr-Coulomb elastoplastic model to simulate the interlayer continuous rock mass, with the structural planes modeled using the built-in joint elements in 3DEC. For homogeneous surrounding rock, the calculation assumes the surrounding rock as an ideal elastoplastic continuum, also adopting the Mohr-Coulomb strength criterion. The model dimensions are shown in the Fig. 7. Additionally, the layer thickness of the layered surrounding rock is set at 1 m, with a tunnel depth of 100 m. The tunnel is designed as a circular shape with a radius of 5 m. The analysis assumes full-face excavation and focuses solely on the self-supporting behavior of the surrounding rock, thus excluding the influence of support structures.

To accurately test the stress distribution after excavation and obtain the shape of the bearing arch, 13 normal measurement lines are uniformly arranged around the tunnel, each measuring 60 m in length and containing 60 measurement points, as shown in Fig. 7. The long tunnel can be regarded as a plane strain problem; therefore, in the longitudinal direction, in addition to applying stress, displacement boundaries are also set to ensure that there is stress without strain in the longitudinal direction.

During the calculations, the initial ground stress equilibrium is first established, and all displacements and accelerations are removed. In the second step, the rock mass elements within the tunnel range are removed, and the system is calculated to equilibrium without changing the boundary conditions.

Table 2 Calculation Conditions

Condition Code	Rock types	Lateral pressure coefficient
A	Homogenous	1
B	Layered	0.5
C		1
D		1.5

3.2.2 Calculation conditions and parameters

In accordance with the test conditions mentioned earlier, the calculation conditions for this study involve the use of various lateral pressure coefficients to control the initial horizontal stress, as outlined in Table 2.

The surrounding rock parameters used in the calculations are based on the values for Class V surrounding rock as specified in China's "Code for Design of Railway Tunnel."

For the parameters of rock contact surface, the author compiled data from the textbook ‘Rock Mechanics’ (Wittke 1990) and related literature (Seedsman 2013, Seedsman 2021, Mao *et al*. 2005, Hu *et al*. 2017, Qin *et al.* 2015, Guo *et al*. 2021). It was found that the normal stiffness of surfaces generally ranges from 1.1 to 16.9 GPa/m, while the shear stiffness typically ranges from 2.2 to 12 GPa/m. Under extreme conditions, such as in contact surfaces containing soft soil or clay, the normal and shear stiffness ranges from 10 to 100 MPa/m. In tightly closed contact surfaces, such as those in basalt, the normal and shear stiffness can exceed 100 GPa/m. Based on the research findings and the author's experience, the selected parameters for contact surfaces are listed in Table 3.

3.2.3 Analysis of bearing arch results

By substituting the stress results at each measurement point on each line in each condition into Eqs. (4) and (5), the stress-bearing capacity of each point can be obtained. The bearing capacity values of 0 and 0.1 on each side line

Table 3 Calculation parameters

Rock parameters							
Rock level	Elastic modulus E/ (GPa)	Poisson ratio	Bulk modulus K/ (GPa)	Shear modulus G/ (GPa)	Volumetric weight D/ (kN/m3)	Cohesion C/ (kPa)	Internal friction angle φ/ (°)
Class V surrounding rock	15	0.35	16.70	5.56	18.50	200	27

Contact surface parameters					
Contact surface	Normal stiffness Kn/ (GPa/m)	Tangential stiffness Ks/ (GPa/m)	Tensile strength Rm/ (kPa)	Cohesion C/ (kPa)	Internal friction angle φ/ (°)
Contact 1	4.5	1.3	1	20	23

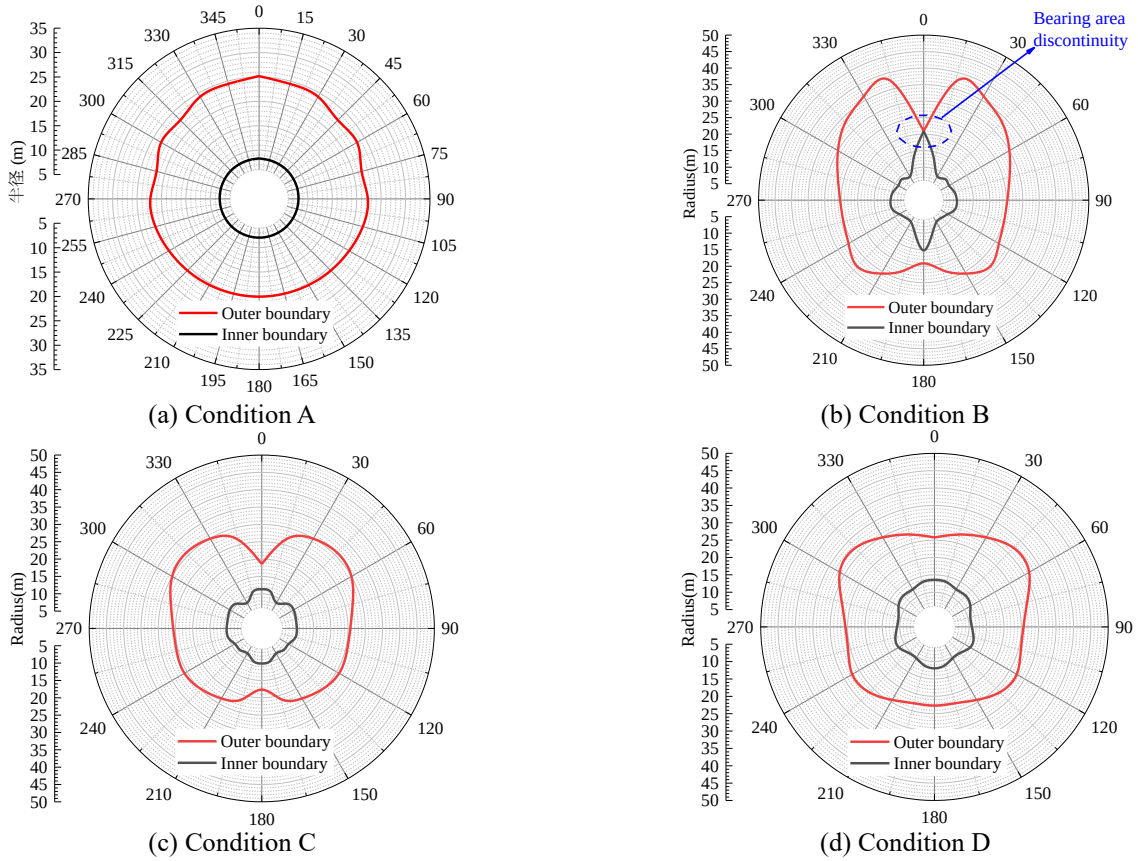

(a) Condition A (b) Condition B

(c) Condition C (d) Condition D

Fig. 8 Range of bearing arches

correspond to the inner and outer boundaries of the load-bearing arch, respectively. By conducting bearing capacity analysis for each condition, the inner and outer boundaries of the load-bearing arch under all conditions can be determined. The load-bearing arch ranges obtained for each calculation condition are shown in Fig. 8.

Comparing the load-bearing arch calculation results between Condition A and Condition C, it can be observed that under the same initial stress conditions, the load-bearing arch in homogeneous rock exhibits a generally regular circular shape, with relatively uniform thickness of the load-bearing arch around the tunnel perimeter. In contrast, the load-bearing arch in layered rock takes on a roughly vertical butterfly shape, with significantly thinner load-bearing arches at the top and bottom.

Comparing the results of Conditions B to D, it is evident that as the initial horizontal stress increases, and influenced by horizontal stress compression, load-bearing regions gradually develop at the top and bottom, leading to a weakening of vertical stress concentration. This corresponds to the findings of the phenomenological tests. When the lateral pressure coefficient is 1.5, which results in the main stress being parallel to the structural surface, the load-bearing regions at the top and bottom become more robust, and the overall shape of the load-bearing arch in the surrounding rock appears to be roughly rounded square. It's worth noting that when the lateral pressure coefficient is 0.5, which makes the main stress direction perpendicular to the structural surface, the inner and outer boundaries of the load-bearing arch at the center of the tunnel's top and

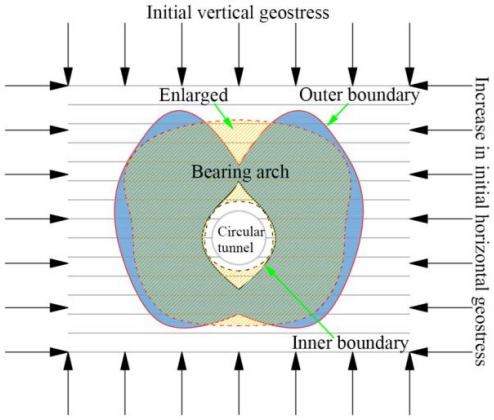

Fig. 9 Morphology of tunnel bearing arch in horizontal layered surrounding rock

bottom tend to overlap, leading to the "bearing area discontinuity" phenomenon as seen in Fig. 8(b).

Based on physical experiments and numerical simulations analyzing the load-bearing mechanism of layered surrounding rock during tunnel excavation, the morphological characteristics of the load-bearing arch in layered rock tunnels are illustrated in Fig. 9. The morphology of the load-bearing arch is significantly influenced by the initial in-situ stress:

When the horizontal stress is relatively low, the vertical stress dominates, compressing the tunnel roof and floor. The load-bearing zones at the roof and floor are significantly smaller than those at the sidewalls, as shown in the blue areas. The overall shape of the load-bearing arch resembles a butterfly, with a core-like inner boundary tangent to the outer boundary at the roof and floor. As horizontal stress increases, the compressive effect of the in-situ stress becomes stronger. As indicated by the dashed lines, both the inner and outer boundaries of the load-bearing arch tend to contract inward. However, under the effect of horizontal compression, the load-bearing area at the tunnel's roof and floor gradually expands, and the overall distribution of the load-bearing arch evolves towards a rounded square shape. The inner boundary transitions from a core-like shape to a uniformly distributed circular form, as indicated by the yellow area in the Fig. 9.

Therefore, when the initial horizontal stress is low, the load-bearing zones at the roof and floor are weaker, making these areas prone to stress concentration. This condition improves as the initial horizontal stress increases.

4. Sensitivity analysis of parameters

From the previous analysis, it is evident that the morphology and distribution characteristics of horizontal layered rock tunnel are primarily influenced by initial ground stress and the physical-mechanical properties of the rock mass. Therefore, this study, in conjunction with numerical simulations, will investigate the impact of variables such as lateral pressure coefficient, layer thickness, and interlayer contact strength on the characteristics of the load-bearing arch.

Table 4 Calculation conditions for layered rock

Condition Code	Lateral pressure coefficient	layer thickness (m)	Interlayer contact
A11	0.50	1.0	Contact 1
A12	0.50	1.0	Contact 2
A21	0.50	2.0	Contact 1
A31	0.50	0.5	Contact 1
B11	0.75	1.0	Contact 1
B12	0.75	1.0	Contact 2
B21	0.75	2.0	Contact 1
B31	0.75	0.5	Contact 1
C11	1.00	1.0	Contact 1
C12	1.00	1.0	Contact 2
C21	1.00	2.0	Contact 1
C31	1.00	0.5	Contact 1
D11	1.25	1.0	Contact 1
D12	1.25	1.0	Contact 2
D21	1.25	2.0	Contact 1
D31	1.25	0.5	Contact 1
E11	1.50	1.0	Contact 1
E12	1.50	1.0	Contact 2
E21	1.50	2.0	Contact 1
E31	1.50	0.5	Contact 1

* The parameter values for Contact 1 can be found in Table 4, and the parameter values for Contact 2 are provided in Table 5

Table 5 Calculation conditions for homogeneous rock

Condition Code	Lateral pressure coefficient
F1	0.50
F2	0.75
F3	1.00
F4	1.25
F5	1.50

Table 6 Parameters for Contact 2

Contact surface	Normal stiffness Kn/ (GPa/m)	Tangential stiffness Ks/ (GPa/m)	Tensile strength Rm/ (kPa)	Cohesion C/ (kPa)	Internal friction angle φ/ (°)
Contact 2	1.1	0.4	1	10	20

4.1 Working conditions and parameter settings

The numerical models in this section were established based on the previous description, and the working conditions are summarized in . Similarly, a homogeneous rock condition was established with different lateral pressure coefficients for comparative analysis, as shown in Table 4.

The rock mass parameters are the same as those listed in Table 3, with the addition of relatively weaker parameters for Contact 2, as shown in Table 6.

4.2 Influence of lateral pressure coefficients

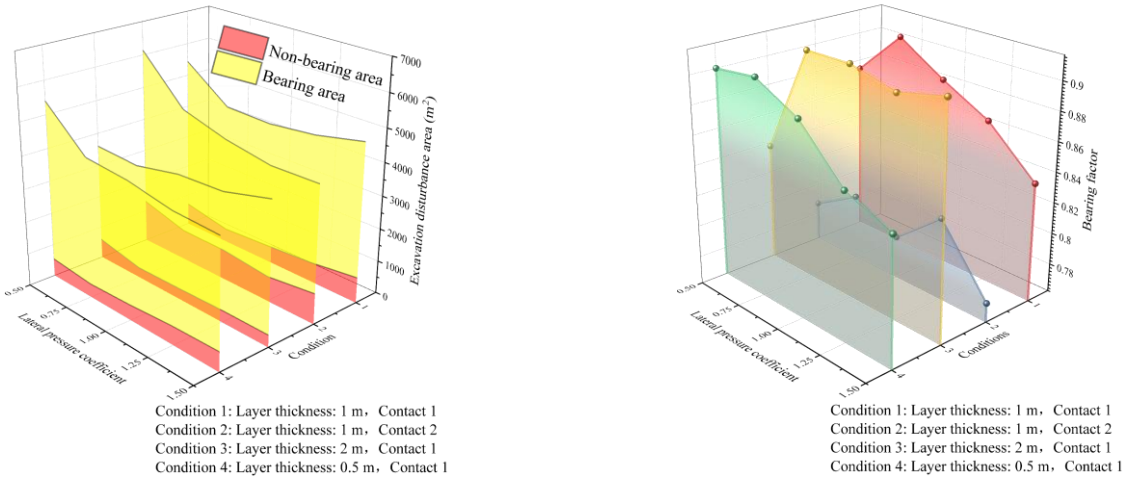

(a) Excavation disturbance area (b) Bearing factor

Fig. 7 Characterisation of the bearing zones at different lateral pressure coefficients

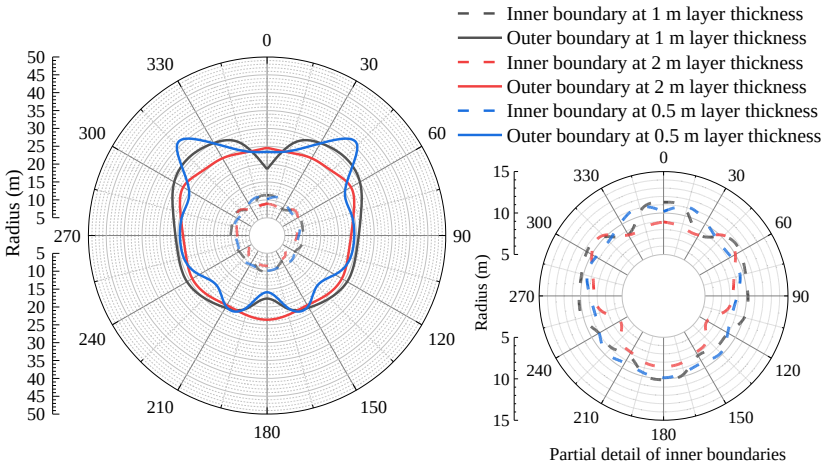

Fig. 11 Range of bearing arches with different layer thicknesses

The previous section analyzed the variation patterns of the bearing arch's shape with different lateral pressure coefficients. To further study the shape and distribution characteristics of the bearing arch under different conditions, this paper defines the bearing factor as the ratio of the bearing area to the excavation-disturbed area.

The excavation-disturbed area is the combined region of the bearing area and non-bearing area. When the bearing factor is close to 1, it signifies a significant proportion of the tunnel structure being within the bearing area, resulting in enhanced safety due to a substantial bearing capability of the surrounding rock. Conversely, a lower bearing factor implies a smaller bearing area and a larger non-bearing area, indicating increased risks due to the disturbance from tunnel excavation.

For specific working conditions, the areas of the bearing zone, non-bearing zone, excavation-disturbed area, and the bearing coefficient were calculated. The results are shown in Fig. 10.

From the excavation-disturbed area chart, it can be observed that for the condition with a 2 m layer thickness and contact 1, the bearing area after excavation increases as the lateral pressure coefficient rises from 0.5 to 1.5, while for other conditions, the bearing area shows a decreasing trend.

Regarding the bearing coefficient, all conditions except for the 1-meter layer thickness with contact type 2 exhibit relatively high bearing coefficients, indicating that interlayer contact significantly affects the excavation disturbance area. It is noteworthy that for the condition with a 2-meter layer thickness and contact type 1, the excavation disturbance area, non-bearing zone, and bearing zone are all at lower levels compared to other conditions, while the bearing coefficient remains high. This suggests that when the layer thickness and interlayer bonding strength reach a certain level, the influence of the layered rock mass on arch formation may weaken, resulting in stronger deformation resistance and self-stabilization capabilities of the surrounding rock.

4.3 Influence of layer thickness

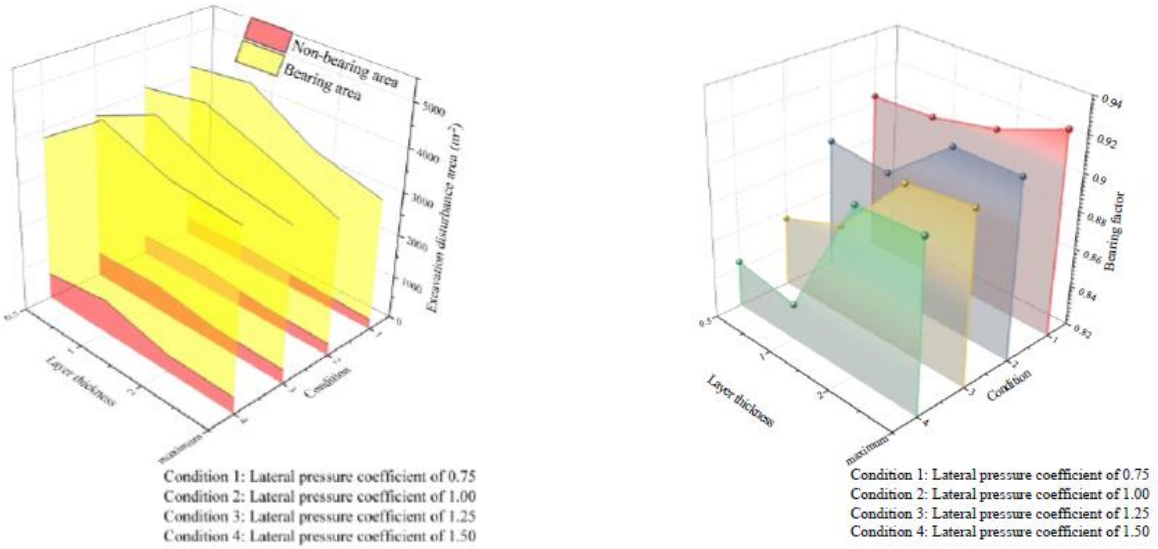

(a) Excavation disturbance area (b) Bearing factor

Fig.12 Characterisation of the bearing zones with different layer thicknesses

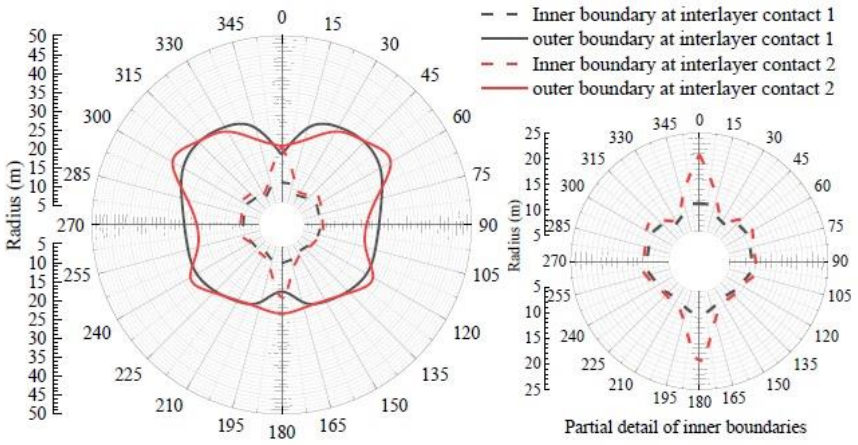

Fig. 13 Range of bearing arches with different interlayer contact conditions

The bearing arch images calculated for specific working conditions are shown in Fig. 11. From the morphology of the bearing arch in horizontally layered surrounding rock, it can be observed that as the layer thickness increases, there are fewer layers in the soil, and the arching effect around the tunnel perimeter is weakened due to the layered structure. Consequently, the inner and outer boundaries of the bearing arch are closer to the excavation profile.

The bearing arch results for different layer thicknesses under contact type 1 conditions were analyzed, with the homogeneous surrounding rock condition considered as an extreme case of "maximum layer thickness" for comparison. The results of various indicators are shown in Fig. 12.

From the Fig. 12, it can be seen that under various lateral pressure coefficient conditions, as the layer thickness increases from 0.5 m to 1.0 m, the area of the non-bearing zone slightly increases, while the bearing area shows a significant increase. The bearing coefficient exhibits an overall increasing trend. This indicates that within this layer thickness range, the surrounding rock achieves stress redistribution and reaches a new equilibrium by transferring stress to deeper layers of the surrounding rock.

In the layer thickness range of 1.0 m to 2.0 m, the influence of joint cutting on the surrounding rock decreases, and the overall strength of the surrounding rock increases. Therefore, the disturbance caused by tunnel excavation on the surrounding rock diminishes, resulting in a reduction of the non-bearing zone area. Additionally, the stress that needs to be balanced by transferring to deeper layers of the surrounding rock also decreases, leading to a reduction in the bearing area. However, the bearing coefficient continues to increase. Overall, as the layer thickness increases, the surrounding rock demonstrates better stability in response to the stress state changes caused by excavation unloading.

4.4 Influence of interlayer bond strength

The bearing arch images under specified conditions for interlayer contacts 1 and 2 are compared and shown in

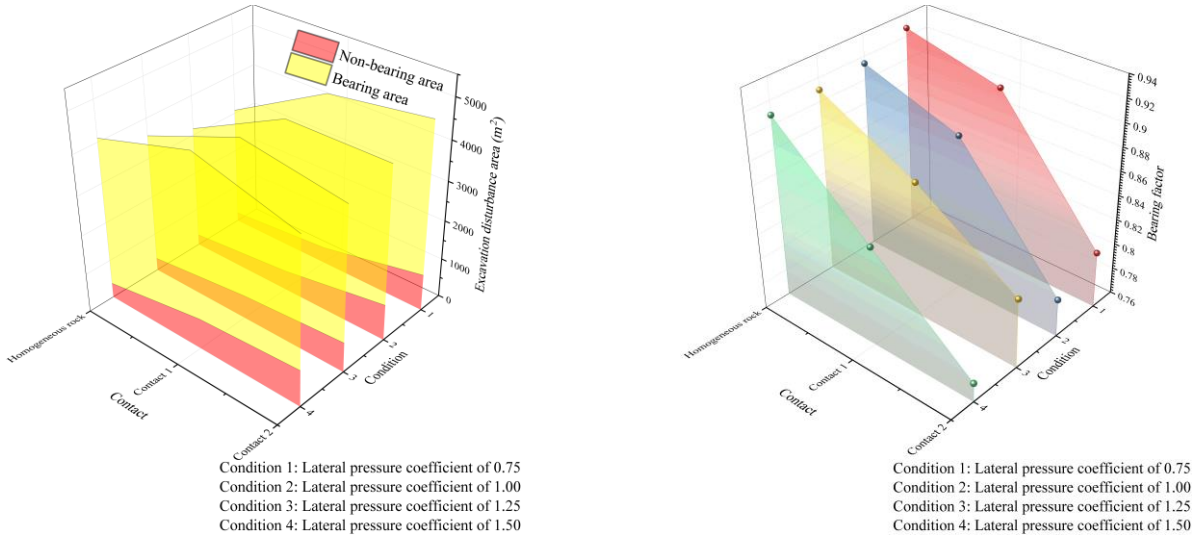

(a) Excavation disturbance area (b) Bearing factor

Fig. 14 Characterisation of the bearing zones with different contact conditions

Fig. 13. From the shape of the bearing arch in the figure, it can be observed that, compared to contact 1, the bearing area under contact 2 with lower bonding strength is significantly smaller, while the non-bearing area is larger, and a discontinuity in the bearing area appears at the crown position.

Regarding different interlayer contacts, a statistical analysis was conducted on various indicators under four lateral pressure coefficients for a layer thickness of 1 meter. The homogeneous surrounding rock condition, considered as the strongest contact scenario with "contact strength equal to the rock mass," was used as a comparison, resulting in Fig. 14.

As shown in the Fig. 14, with the deterioration of interlayer contact, the ability of the layered surrounding rock to cope with tunnel excavation disturbances weakens. The disturbance area after tunnel excavation shows little change, while the non-bearing zone area expands, and the bearing zone area decreases. The changes in the bearing coefficient indicate that the results of the excavation disturbance pose significant safety risks.

It can be seen that changes in interlayer contact have a relatively small impact on the disturbance area caused by tunnel excavation but have a significant effect on the changes in the bearing coefficient. This indicates that interlayer contact primarily affects the distribution of stress during the stress redistribution process, particularly its impact on the internal boundary. When interlayer contact is good, more stress is transferred to the deeper parts of the surrounding rock to achieve equilibrium. In contrast, when interlayer contact is poor, the surrounding rock tends to release stress through deformation to achieve stress balance, ultimately determining the state of stress redistribution.

Therefore, based on the physical experiments and sensitivity analysis of numerical simulation parameters, it can be concluded that in tunnel engineering within horizontally layered surrounding rock, engineering measures should aim to enhance the overall integrity of the surrounding rock. Examples include applying enhanced support to the roof and floor to address interlayer compressive and tensile failures, improving interlayer bonding strength through grouting to reduce the non-load-bearing zone area, and adopting additional reinforcement measures, such as installing reinforced meshes or prestressed rock bolts (cables), in strata with poor bonding strength. During construction, real-time monitoring data should be utilized to fully leverage the load-bearing arch effect and dynamically refine excavation sequences and support strategies.

5. Conclusions

Through testing and numerical simulations, this paper analyzes the distribution patterns of the bearing arch in the excavation of horizontal laminated surrounding rock caverns from various perspectives. For comparison, homogeneous surrounding rock conditions were also considered, leading to the following key conclusions:

In heterogeneous rock masses, structural planes can cause structural deformations under unfavorable stress conditions. This can lead to rock layer failures, such as bending, at stress levels significantly lower than the ultimate strength of the rock blocks. In tunnel excavation within horizontally layered surrounding rock, vertical loads are considered unfavorable because they induce tensile stress due to bending in the roof and floor. On the other hand, an increase in initial horizontal stress can improve conditions to some extent, promoting a more even distribution of stress concentration around the tunnel perimeter and forming a load-bearing arch at the roof and floor positions.

After tunnel excavation, the bearing arch morphology in horizontal laminated surrounding rock exhibits two extreme states: "butterfly-shaped" and "rounded-square." Under favorable boundary conditions, the arch assumes a "rounded-square" shape. As boundary conditions deteriorate, the arch gradually transforms into a "butterfly-

shaped" configuration, and in some cases, may even show a "bearing area discontinuity" in the vertical direction.

The side pressure coefficient and interlayer bonding strength significantly impact the bearing arch, whereas the effect of layer thickness is relatively minor:

As the side pressure coefficient increases, under the compression effect of horizontal stress, bearing arches form near the tunnel's roof and floor. When the side pressure coefficient is within the range of 0.75 to 1.25, the surrounding rock stability after tunnel excavation is relatively good.

During the transition from thin to thick layers, the unloading stability of the surrounding rock during excavation improves. When the layer thickness is between 0.5 m and 1 m, the disturbed area of excavation increases, but the bearing arch area also expands, with stress being balanced by transferring it to deeper surrounding rock. When the layer thickness exceeds 1 m, the disturbed area of excavation significantly decreases, and the stress needing to be transferred to deeper surrounding rock reduces, indicating a diminished influence of layering at this point.

Interlayer contacts have a limited effect on the total disturbed area of excavation but significantly influence the distribution between bearing and non-bearing zones. When interlayer contacts are strong, the non-bearing zone is smaller, allowing more stress to be transferred to deeper surrounding rock to achieve equilibrium. Conversely, when interlayer contacts are weak, the non-bearing zone area increases significantly, and the surrounding rock tends to release stress through deformation to reach equilibrium.

In the design and construction of tunnels in horizontally layered surrounding rock, engineering measures should focus on enhancing the overall integrity of the surrounding rock. Future research could explore the load-bearing arch characteristics under different geological conditions, such as inclined layered or complex jointed rock masses, to provide more targeted guidance for tunnel engineering.

Acknowledgments

This research was supported by the National Natural Science Foundation of China (grand No. 52478416), for which the authors are grateful. The authors also sincerely appreciate the profound and valuable comments provided by the anonymous reviewers of this paper.

References

Brady, B. and Brown, E. (1985), Rock mechanics for underground mining. George Allen & Unwin (Publishers) Ltd, London.

Chen, Z., He, C., Wang, B., Yuan, Q., Jiang, C., Yuan, S. and Wang, X. (2024), "experimental investigation on failure mechanism and rockburst process of tunnels under different span-ratios and existing structural planes", *Rock Mech. Rock Eng*., 1-23. https://doi.org/10.1007/s00603-024-03767-z.

Chen, Z., He, C., Wang, J. and Ma, C. (2021), "Time-dependent squeezing deformation mechanism of tunnels in layered soft-rock stratum under high geo-stress", *J. Mountain Sci*., **18**(5), 1371-1390. https://doi.org/10.1007/s11629-020-6356-0

Do, N.A., Dias, D., Tran, T.T., Dao, V.C., Dao, V.D. and Nguyen, P.N. (2019), "Behavior of noncircular tunnels excavated in stratified rock masses–Case of underground coal mines", *J. Rock Mech. Geotech. Eng*., **11**(1), 99-110. https://doi.org/10.1016/j.jrmge.2018.05.005.

Guo, Z., Fan, J., Wang, F., Zhou, H. and Li, W. (2021), "Geomechanical model experiment study on deformation and failure mechanism of the mountain tunnel in layered jointed rock mass", *Adv. Civil Eng*., 1-19. https://doi.org/10.1155/2021/6645124

Hoek, E. and Brown, E. (1980), Underground excavations in rock. The Institute of Mining and Metallurgy, London.

Hu, S., Tan, Y., Zhou, H., Guo, W., Hu, D., Meng, F. and Liu, Z. (2017), "Impact of bedding planes on mechanical properties of sandstone", *Rock Mech. Rock Eng*., **50**, 2243-2251. https://doi.org/10.1007/s00603-017-1239-6

Huang, X., Ruan, H., Shi, C. and Kong, Y. (2021), "Numerical simulation of stress arching effect in horizontally layered jointed rock mass", *Symmetry*, **13**(7), 1138. https://doi.org/10.3390/sym13071138.

Jin, C., Shao, A., Liu, D., Han, T., Fan, F. and Li, S. (2018), "Failure mechanism of highly stressed rock mass during unloading based on the stress arch theory", *Int. J. Geomech*., **18**(11), 04018146. https://doi.org/10.1061/(ASCE)GM.1943-5622.0001280.

Khezri, N., Mohamad, H. and Fatahi, B. (2016), "Stability assessment of tunnel face in a layered soil using upper bound theorem of limit analysis", *Geomech. Eng*., **11**(4), 471-492. https://doi.org/10.12989/gae.2016.11.4.471.

Lei, M., Peng, L. and Shi, C. (2015), "Model test to investigate the failure mechanisms and lining stress characteristics of shallow buried tunnels under unsymmetrical loading", *Tunn. Undergr. Sp. Tech*., **46**, 64-75. https://doi.org/10.1016/j.tust.2014.11.003.

Li, P., Chen, Y., Huang, J., Wang, X., Liu, J. and Wu, J. (2023), "Design principles of prestressed anchors for tunnels considering bearing arch effect", *Comput. Geotech*., **156**, 105307. https://doi.org/10.1016/j.compgeo.2023.105307.

Lin, X., Chen, R., Wu, H.N., Meng, F.Y. and Su, D. (2022), "Calculation of earth pressure distribution on the deep circular tunnel considering stress-transfer mechanisms in different zones", *Tunn. Undergr. Sp. Tech*., **119**, 104211. https://doi.org/10.1016/j.tust.2021.104211.

Ma, K., Zhang, J., Dai, Y., Kong, C., Zhou, P. and Xu, Q. (2022), "The calculation for ultimate surrounding earth pressure on deep-buried tunnels in aeolian sand stratum to prevent surface collapse", *Bull. Eng. Geol. Environ*., **81**(9), 390. https://doi.org/10.1007/s10064-022-02894-7.

Ma, K., Zhang, J., Zhang, J., Dai, Y. and Zhou, P. (2022), "Floor heave failure mechanism of large-section tunnels in sandstone with shale stratum after construction: A case study", *Eng. Fail. Anal*., **140**, 106497. https://doi.org/10.1016/j.engfailanal.2022.106497.

Ma, K., Zhang, J., Zhang, J., Feng, J., Zhou, P. and Kong, C. (2024), "Determination of the rock mass bearing mechanism following excavation of circular tunnels", *Rock Mech. Rock Eng*., 1-18. https://doi.org/10.1007/s00603-024-03840-7.

Małkowski, P. (2015), "The impact of the physical model selection and rock mass stratification on the results of numerical calculations of the state of rock mass deformation around the roadways", *Tunn. Undergr. Sp. Tech*., **50**, 365-375. https://doi.org/10.1016/j.tust.2015.08.004.

Man, J., Zhou, M., Zhang, D., Huang, H. and Chen, J. (2022), "Face stability analysis of circular tunnels in layered rock masses using the upper bound theorem", *J. Rock Mech. Geotech. Eng*., **14**(6), 1836-1848. https://doi.org/10.1016/j.jrmge.2021.12.023.

Mao, H. and Yang, C. (2005), "Study on effects of discontinuities on mechanical characters of slate", *Chinese J. Rock Mech. Eng*.,

24(20), 3651-3656. (in Chinese).
Moussaei, N., Sharifzadeh, M., Sahriar, K. and Hossein Khosravi, M. (2019), "A new classification of failure mechanisms at tunnels in stratified rock masses through physical and numerical modeling", *Tunn. Undergr. Sp. Tech*., **91**, 103017. https://doi.org/10.1016/j.tust.2019.103017.
Pardo, G.S. and Sáez, E. (2014), "Experimental and numerical study of arching soil effect in coarse sand", *Comput. Geotech*., **57**, 75-84. https://doi.org/10.1016/j.compgeo.2014.01.005.
Qin, C.B., Yang, X.L., Pan, Q.J., Sun, Z.B., Wang, L.L. and Miao, T. (2015), "Upper bound analysis of progressive failure mechanism of tunnel roofs in partly weathered stratified Hoek–Brown rock masses", *Int. J. Rock Mech. Min. Sci*., **74**, 157-162. https://doi.org/10.1016/j.ijrmms.2014.10.002.
Rodriguez, R. and Perez, F. (2021), "Carbon foot print evaluation in tunneling construction using conventional methods", *Tunn. Undergr. Sp. Tech.*, **108**, 103704. https://doi.org/10.1016/j.tust.2020.103704.
Seedsman, R. (2013), "Practical strength criterion for coal mine roof support design in laminated soft rocks", *Min. Technol*., **122**(4), 243-249.
Seedsman, R. (2021), "Assessing the conditions at the boundary of excavations in bedded or foliated rocks", *Int. J. Rock Mech. Min. Sci*., **148**, 104983. https://doi.org/10.1016/j.ijrmms.2021.104983.
Tan, Y., Liu, Y. and Li, Z. (2014), "The proper width of the intermittent trough for tunnel enlarging", *Geomech. Eng*., **6**(5), 455-467. https://doi.org/10.12989/gae.2014.6.5.455.
Wang, F., Chen, T., Ma, B. and Chen, D. (2022), "Formation mechanism of stress arch during longwall mining based on key strata theory", Energ. Explor. Exploit., **40**(2), 816-833. https://doi.org/10.1177/01445987211042701.
Wittke, W. (1990), Rock Mechanics. Springer-Verlag, Berlin.
Yang, X. and Li, K. (2016), "Roof collapse of shallow tunnel in layered Hoek-Brown rock media", *Geomech. Eng*., **11**(6), 867-877. https://doi.org/10.12989/gae.2016.11.6.867.
Yang, X.L. and Zhang, R. (2017), "Collapse analysis of shallow tunnel subjected to seepage in layered soils considering joined effects of settlement and dilation", *Geomech. Eng*., **13**(2), 217-235. https://doi.org/10.12989/gae.2017.13.2.217.
Yanli, Q., Shaoquan, W., Mingzhou, B., Hai, S., Pengxiang, L., Hao, Z. and Bohu, H. (2021), "Evaluation and deformation control study on the bias pressure of layered rock tunnels", *Math. Probl. Eng*., 9937678. https://doi.org/10.1155/2021/9937678.
Yuan, Y., Han, C., Zhang, N., Feng, X., Wang, P., Song, K. and Wei, M. (2022), "Zonal disintegration characteristics of roadway roof under strong mining conditions and mechanism of thick anchored and trans-boundary supporting", *Rock Mech. Rock Eng*., 1-19. https://doi.org/10.1007/s00603-021-02653-2.
Zhao, Z., Jing, H., Shi, X., Yang, L., Yin, Q. and Gao, Y. (2021), "Study on bearing characteristic of rock mass with different structures: Physical modeling", *Geomech. Eng*., **25**(3), 179-194. https://doi.org/10.12989/gae.2021.25.3.179.
Zhu, Z.,Fang, Z., Xu, F., Han, Z., Guo, X. and Ma, C. (2022), "Model test study on the rock mass deformation law of a soft rock tunnel under different ground stresses", *Front. Earth Sci*., **10**, 962445. https://doi.org/10.3389/feart.2022.962445.